

# Modeling Oxygen Loss and Phase Transformation in Ni-Rich Cathode Materials: Impact of Electrode Microstructure

Svenja Both,<sup>[a, b]</sup> Simon Hein,<sup>[a, b]</sup> Timo Danner,<sup>\*[a, b]</sup> and Arnulf Latz<sup>[a, b, c]</sup>

Nickel-Manganese-Cobalt (NMC) oxides are widely used as cathode materials in lithium-ion batteries. While increasing the nickel content increases the available capacity in a given voltage window, it also reduces the structural stability of the material when cycled to high cutoff voltages. Oxygen release from the crystal structure as well as a layered-to-rocksalt phase transformation of the layered oxide material cause capacity loss and impedance rise. In this work, we propose a continuum approach to model oxygen release and the associated phase

transformation using a 1+1D model informed by atomistic simulations to predict the thickness of reconstructed active material over time. An efficient interface model allows us to combine this approach with 3D microstructure-resolved simulations in order to study the effect of a resistive layer on a real cathode microstructure. This novel workflow enables us to investigate the effect of individual electrode properties on the phase transformation and guide future electrode design.

## 1. Introduction

Ni-rich layered oxide materials are widely used as cathode materials in lithium-ion batteries. While increasing the Nickel content in those Nickel-Manganese-Cobalt (NMC) stoichiometries increases the available capacity in a given voltage window,<sup>[1,2]</sup> it also poses challenges to the structural stability of the material. Especially when cycled to a high cutoff voltage, capacity fade and impedance buildup have been observed experimentally.<sup>[3–7]</sup> One major cause of degradation in Ni-rich cathode materials is known to be a release of oxygen from the structure at very low degrees of lithiation<sup>[1,4,8,9]</sup>, ultimately leading to a spinel and/or rocksalt structure.<sup>[3,7,10–13]</sup> While a spinel-phase still allows for Lithium diffusion,<sup>[14]</sup> the presence of a Ni-rich rocksalt phase is known to induce sluggish lithium kinetics, thus significantly increasing the intercalation overpotential as well as inhibiting lithium diffusion in the crystal structure.<sup>[7,13,14]</sup> This leads to an increased cathode overpotential as well as an increased charge-transfer resistance often observed in electrochemical impedance spectroscopy.<sup>[3,5]</sup> It was further proposed to limit the achievable capacity due to a

“pinning” effect of the rocksalt crystal structure on the still intact inner NMC structure.<sup>[15]</sup>

Different techniques have been applied experimentally to study oxygen loss from the crystal structure, mainly online electrochemical mass spectrometry.<sup>[1,4,8,16–18]</sup> Different groups successfully applied this measurement technique, which was also used to study commercial large format pouch cells.<sup>[19]</sup> Studies have shown a distinct onset of oxygen release for stoichiometries of NMC811 and above at approx. 80% SOC.<sup>[1,2,20,21]</sup> Dose et al. further showed a dependency of the electrolyte system on the process.<sup>[8,16]</sup> Due to the high reactivity of the released oxygen,<sup>[20]</sup> follow-up reactions with the electrolyte<sup>[24,8,22]</sup> are suggested that lead to electrolyte consumption and possibly formation of acidic species.<sup>[22]</sup>

The spinel- or rocksalt phase on the particle surface is usually investigated using high-resolution imaging techniques like transmission electron microscopy (TEM).<sup>[3,7,8,10,23–26]</sup> Reported reconstruction layer thicknesses depend among other factors on the material, the cycling or storage conditions and the electrolyte. For NMC, the thickness of the reconstructed layer has been reported to be a few nanometers,<sup>[3,7,8,10]</sup> 15–20 nm,<sup>[3,27]</sup> 25 nm<sup>[23,25,28]</sup> as well as between 30 nm and 50 nm<sup>[12,13,26,27]</sup>. However, surface reconstruction is not limited to NMC but has been reported in NCA as well.<sup>[29,30]</sup>

While a lot of work has been carried out experimentally to understand the degradation of NMC materials, only a few modeling studies exist in the literature trying to predict oxygen loss and phase transformation. On the molecular scale, several studies investigate the mechanisms of oxygen release from Li-rich and Ni-rich crystal structures, which is directly connected to the phase transformation process. Oxygen loss has been attributed to a strong covalency of the transition metal-oxygen bonds<sup>[31,32]</sup> due to hybridization of the oxygen 2p and transition metal 3d orbitals.<sup>[31]</sup> Genreith-Schriever et al. use different computational tools such as density functional theory (DFT) and ab-initio molecular dynamics simulations to investigate the oxygen loss mechanism in  $\text{LiNiO}_2$ .<sup>[31]</sup> They suggest a mechanism

[a] S. Both, Dr. S. Hein, Dr. T. Danner, Prof. Dr. A. Latz  
German Aerospace Center (DLR), Institute of Engineering Thermodynamics,  
Stuttgart, Germany  
E-mail: timo.danner@dlr.de

[b] S. Both, Dr. S. Hein, Dr. T. Danner, Prof. Dr. A. Latz  
Helmholtz Institute Ulm for Electrochemical Energy Storage (HIU),  
Ulm, Germany

[c] Prof. Dr. A. Latz  
Institute of Electrochemistry, Ulm University,  
Ulm, Germany

Supporting information for this article is available on the WWW under <https://doi.org/10.1002/batt.202400802>

© 2025 The Author(s). Batteries & Supercaps published by Wiley-VCH GmbH. This is an open access article under the terms of the Creative Commons Attribution License, which permits use, distribution and reproduction in any medium, provided the original work is properly cited.

via peroxide formation and subsequent oxidation to  $O_2$  on the (012)-facet with a significant role of oxygen redox in the delithiation process. Kong et al. propose an oxygen dimerization on the (104)-facet of  $LiNiO_2$ , while oxygen loss in the bulk is kinetically prohibited.<sup>[32]</sup> They also provide the formation energy of oxygen vacancies, that decreases with state of delithiation.<sup>[32]</sup> Similar vacancy calculations for Ni-rich materials suggested in the literature show a significant dependency of the state of lithiation in the active material<sup>[11,33,34]</sup> and will be used in our modeling framework.

On the continuum scale, Ghosh et al. have formulated a shrinking-core model with a moving boundary between intact NMC and degraded shell once a distinct state of delithiation is reached.<sup>[35]</sup> They showed the functionality of their model in a single particle model, which was later extended to a volume-averaged p2D model.<sup>[36]</sup> Furthermore, Zhuang derived a free energy degradation model of cation-disorder based on first-principle considerations.<sup>[37]</sup> An analysis of the impact of structural parameters on the growth of a rocksalt phase on the particle surface and its impact on the performance of commercial cathode architectures is not reported in the literature so far. Therefore, we will present a novel modeling approach to describe phase transformation and oxygen release in a volume-averaged 1+1D model informed by atomistic simulations of oxygen vacancy formation. This model is combined with a resistive interface model in our 3D microstructure-resolved simulations to investigate the impact of a resistive layer at the particle surface on a real electrode microstructure. Validation of our homogenized 1+1D model with our 3D simulations allows us to qualitatively study the effect of microstructural properties on electrode degradation. This unique workflow allows us to study important design

parameters for electrode manufacturing in order to optimize cathode design.

## 2. Modeling Approach

In this section we present a physico-chemical model describing the growth of a rocksalt phase and its impact on electrochemical processes on the particle surface. On the one hand, the model is designed to capture the key rate-determining processes and is informed by the results of atomistic simulations. On the other hand, the model formulation also aims at efficiency allowing for future implementation in a 3D numerical framework for microstructure-resolved simulations.

An overview of the simulation workflow is presented in Figure 1. We start off from the commercial Ni-rich cathode microstructure obtained through FIB-SEM, that was discussed in our previous work.<sup>[38]</sup> We want to capture the electrochemical performance as accurately as possible by our volume-averaged 1+1D model in order to simulate the film thickness growth over several cycles while ensuring realistic model predictions. To do so, we extract all relevant microstructure parameters like specific surface area, material volume contents, particle size distribution as well as effective transport properties from the electrode as discussed in the Model Parametrization Section. Furthermore, all model parameters are summarized in the Supporting Information. We validate the rate performances obtained with the 1+1D model by comparing them to 3D microstructure-resolved simulations in the pristine state, i.e. prior to cycling. The phase transformation is then simulated using the 1+1D approach, which yields a film thickness that is spatially resolved across the electrode. As indicated in Figure 1, we can use this thickness profile as input for the resistive film

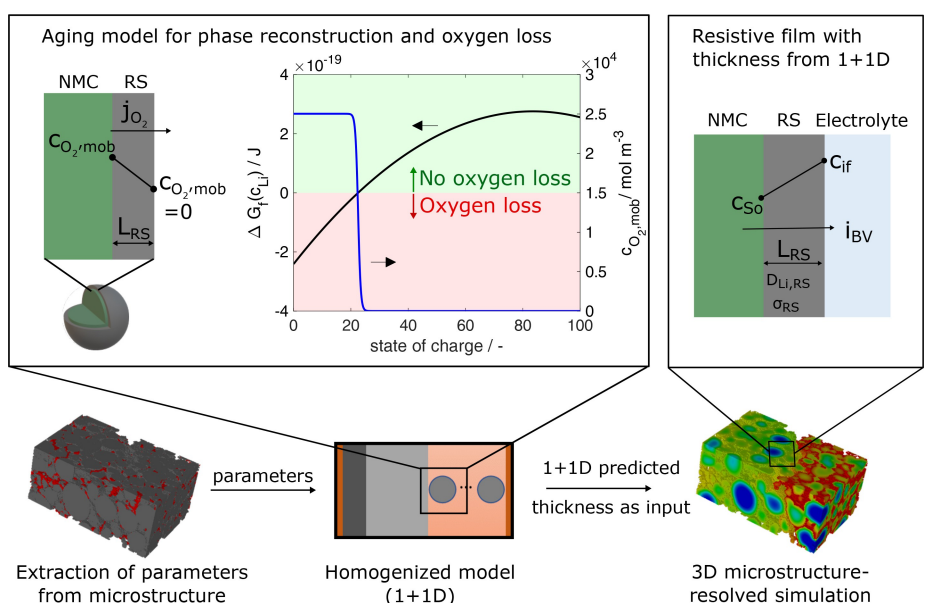


**Figure 1.** Schematic depiction of our workflow. Starting from a realistic microstructure<sup>[38]</sup> (FIB-SEM), all relevant geometrical parameters are extracted and transferred to the 1+1D approach. Our aging model predicts a reconstructed layer thickness due to oxygen formation, which can be used as input for our microstructure-resolved simulation with a resistive film.

model described in Section 2.1 that has been implemented in our 3D microstructure-resolved framework. Note that in the current workflow we include only a weak coupling between rocksalt phase formation and electrochemical performance in the 3D simulations since the growth process is simulated in the 1+1D model only. In future work we plan to simulate rocksalt phase formation in the 3D domain, thereby directly coupling the growth process with internal concentrations and potential fields in the complex 3D microstructure. In the subsequent paragraphs we first present the interface model for rocksalt phase formation. In the final paragraph of this section we will then explain coupling to the 3D cell scale simulation.

## 2.1. Interface Model for Rocksalt Phase Formation

In our modeling approach, we assume an inner core of intact bulk NMC material with a layer of oxygen depleted phase at the surface of the particle. The transformed phase is reported to be either a spinel structure, a rocksalt structure or a mix between the two aforementioned. A thermodynamic driving force exists to separate the layered structure into rocksalt and oxygen gas at very low states of lithiation<sup>[14]</sup> and the rocksalt can also be considered as a lower limit for both Li diffusion and available Li sites in the structure. Full rocksalt growth further raises the question of the ability of Li-ions to diffuse through this phase. A metal-rich phase with Ni occupation of octahedral sites would lead to significantly reduced Li ion transport channels<sup>[14]</sup> and thus significantly reduced diffusion of Li ions while a spinel-phase still allows for Li site-hopping.<sup>[14]</sup> Jung et al. propose a more spot-like growth of a rocksalt phase depending on the cutoff voltage of the cycling protocol.<sup>[3]</sup> Therefore, even though we refer to the evolved phase as "rocksalt" in the manuscript, we consider it as a probably mixed phase that still allows for Li-ion diffusion or a non-uniform phase with pristine spots which still allow for intercalation. Note that our model framework leads to uniform growth of the layer around the spherical particle in the 1+1D model. Spot-like growth could be captured by implementation of our model in the fully 3D-resolved framework and will be subject to future work.

In the following sections we will introduce the two individual models of our rocksalt growth model as shown in Figure 1, namely the growth over time in the 1+1D model as well as the interface model to combine it with microstructure-resolved simulations.

### 2.1.1. Film Thickness Growth

First, we assume that per mole oxygen leaving the intact NMC, two moles of rocksalt (RS) phase are being formed taking into account the stoichiometry of intact NMC as well as pure rocksalt NiO.



The RS layer is assumed to be of thickness  $L_{\text{RS}}$  and grows over time due to the oxygen flux  $\vec{j}_{\text{O}_2}$ .

$$\frac{dL_{\text{RS}}}{dt} = \frac{V_{\text{RS}}}{v_{\text{stoich}}} \cdot \vec{j}_{\text{O}_2} \cdot \vec{n} \quad (2)$$

with  $V_{\text{RS}}$  as the molar volume of the rocksalt phase and  $v_{\text{stoich}}$  as the stoichiometric coefficient from Eq.(1) and the surface normal  $\vec{n}$  pointing out of the particle. We model the oxygen flux through the RS phase using Fick's first law of diffusion in one dimension with a constant oxygen diffusion coefficient. The concentration of mobile oxygen at the interface between NMC and rocksalt is denoted with  $c_{\text{O}_2,\text{mob}}$ . Due to the high reactivity of the evolved oxygen, which is often reported to be in its singlet state,<sup>[22,20,31]</sup> we assume the mobile concentration at the outer surface to be zero due to instantaneous follow-up reactions with the electrolyte. This leads to the simplified equation for the oxygen flux given by Eq. (3).

$$\vec{j}_{\text{O}_2} \cdot \vec{n} = -D \frac{\partial c}{\partial x} \cdot \vec{n} \approx D_{\text{ox}} \frac{c_{\text{O}_2,\text{mob}}}{L_{\text{RS}}} \cdot \vec{n} \quad (3)$$

The concentration of mobile oxygen at the interface NMC-RS can be calculated based on the formation energy of an oxygen vacancy in the NMC crystal as computed from Density Functional Theory (DFT).  $\Delta G_f(c_{\text{Li}})$  is the formation energy of an oxygen vacancy in the crystal. Since it is well-known that this formation energy depends on the state of lithiation with a significantly reduced energy needed to form the vacancy (and thereby a mobile oxygen species) at low states of lithiation,<sup>[33,34,39]</sup> we consider it to be dependent on the Li concentration in NMC. A fit to literature data<sup>[11,33,34]</sup> is used in the present work and shown in Figures 1 and S1a), which acts as a starting point for refined approaches in the future. The formation energy  $\Delta G_f(c_{\text{Li}})$  of an oxygen vacancy is calculated according to the following function of state-of-charge (soc):

$$\Delta G_f(c_{\text{Li}}) = p_1 \cdot \text{soc}^2 + p_2 \cdot \text{soc} + p_3 \quad (4)$$

with the coefficients  $p_1$ ,  $p_2$  and  $p_3$  given in the Supporting Information. Note that soc in Eq. (4) is defined between 0 for a fully delithiated cathode material and 100 for a fully lithiated cathode. From the DFT-based energy of vacancy formation, one can calculate the number of oxygen vacancies in a crystal in equilibrium:

$$N_{\text{vac}} = (N_{\text{sites}} - N_{\text{vac}}) \exp\left(\frac{-\Delta G_f(c_{\text{Li}})}{k_B T}\right) \quad (5)$$

with  $N_{\text{vac}}$  as the total number of vacancies,  $N_{\text{sites}}$  as the total number of sites,  $\Delta G_f(c_{\text{Li}})$  as the formation energy of vacancies and the product of the Boltzmann constant  $k_B$  and temperature  $T$ . Rearranging this equation for the number of vacancies yields:

$$N_{\text{vac}} = \frac{N_{\text{sites}} \cdot \exp\left(\frac{-\Delta G_f(c_{\text{Li}})}{k_B T}\right)}{1 + \exp\left(\frac{-\Delta G_f(c_{\text{Li}})}{k_B T}\right)} \quad (6)$$

The total number of sites can be calculated according to  $N_{\text{sites}} = N_A \cdot n_{O_2}$  with the Avogadro constant  $N_A$  and the amount of oxygen atoms  $n_{O_2}$ . One mole Li(NMC)O<sub>2</sub> contains one mole dimolecular oxygen O<sub>2</sub>. This leads to:

$$N_{\text{sites}} = N_A \cdot n_{\text{NMC}} = N_A \cdot \frac{\rho_{\text{NMC}} V_{\text{NMC}}}{M_{\text{NMC}}} \quad (7)$$

with  $\rho_{\text{NMC}}$  as the crystallographic density of NMC, the volume of NMC  $V_{\text{NMC}}$  and the molar mass  $M_{\text{NMC}}$ . The quotient  $\rho_{\text{NMC}}/M_{\text{NMC}}$  can also be expressed as the maximum concentration  $c_{\text{Li,max}}$ . Using Eq. (7) in Eq. (6) and dividing by the Avogadro number  $N_A$  and the NMC volume  $V_{\text{NMC}}$  yields the concentration of mobile oxygen.

$$c_{O_2,\text{mob}} = \frac{c_{\text{Li,max}} \cdot \exp\left(\frac{-\Delta G_f(c_{\text{Li}})}{k_B T}\right)}{1 + \exp\left(\frac{-\Delta G_f(c_{\text{Li}})}{k_B T}\right)} \quad (8)$$

with  $c_{\text{Li,max}}$  as the total number of sites in the oxygen lattice, which will be further denoted as  $c_{\text{ox,lattice}}$ . Since the phase change to MO according to Eq. (1) is assumed, only half the oxygen can be extracted during the phase transformation. Therefore, we set the maximum concentration of lattice sites to half of the maximum Li concentration. Both the formation energy  $\Delta G_f(c_{\text{Li}})$ , that is dependent on the state of lithiation, as well as the resulting mobile oxygen concentration from Eq. (8) are shown in Figures 1 and S1. The mobile concentration of oxygen is close to its maximum value for a very low state of lithiation (i.e. formation energy of oxygen vacancies below 0) and close to 0 for high states of lithiation. Hence, the phase growth is always greater than or equal to zero.

From Eqs. (2), (3) and (8) it follows that the total film thickness growth over time can be calculated using Eq. (9).

$$\frac{dL_{\text{RS}}}{dt} = \frac{V_{\text{RS}} c_{\text{ox,lattice}} D_{\text{ox}}}{L_{\text{RS}} v_{\text{stoich}}} \frac{\exp\left(\frac{-\Delta G(c_{\text{Li}})}{k_B T}\right)}{1 + \exp\left(\frac{-\Delta G(c_{\text{Li}})}{k_B T}\right)} \quad (9)$$

Given the form of this differential equation, the thickness will evolve with the square root of time. This will be further discussed in the Results Section.

### 2.1.2. Resistive Layer

As we are now able to calculate the thickness of the layer over time, we follow the modeling approach for a resistive film by Clausnitzer et al.<sup>[40]</sup> The film induces an additional voltage drop and a concentration polarization. The faradaic current is modeled using a Butler-Volmer approach given by Eq. (10).

$$i_{\text{BV}} = 2 i_{00} c_{\text{El}}^{0.5} c_{\text{if}}^{0.5} (c_{\text{Li,max}} - c_{\text{if}})^{0.5} \sinh\left(\frac{F}{2RT} \eta\right) \quad (10)$$

The voltage drop results from charge-transfer kinetics, in which the overpotential  $\eta$  can be described as:

$$\eta = \Phi_s - \varphi_e - U_0(c_{\text{if}}) - R_{\text{RS}} i_{\text{BV}} \quad (11)$$

with  $R_{\text{RS}} i_{\text{BV}}$  as an additional term due to the assumed resistive film. Note that the Butler-Volmer current in Eq. (10) depends on itself and is therefore an additional unknown. More information on this aspect can be found in the Supporting Information. The resistance of the film depends on both the thickness as well as its electronic conductivity.

$$R_{\text{RS}} = \frac{L_{\text{RS}}}{\sigma_{\text{RS}}} \quad (12)$$

Furthermore, the concentration at the interface  $c_{\text{if}}$  depends on the solid concentration at the active material-electrolyte interface, the local current, the film thickness, the Faraday constant as well as the diffusion coefficient of Li in the resistive layer.

$$c_{\text{if}} = c_{\text{so}} - \frac{i_{\text{BV}} L_{\text{RS}}}{F D_{\text{Li,RS}}} \quad (13)$$

We do not spatially resolve the growing film, but take into account its impact as a surface variable as the film itself is very thin (nm) compared to the particle size ( $\mu\text{m}$ ). Note that this approach in the 3D microstructure-resolved simulation currently only takes into account interfaces between active material and electrolyte and not the interfaces between porous carbon-binder-domain (CBD) and active material.

## 2.2. Electrochemical Models

In order to focus on the cathode, we study half-cells using a setup of a Li counter electrode, a homogenized separator and the cathode of interest. We calculate the layer growth in a homogenized 1+1D (P2D) model<sup>[41]</sup> developed in an in-house Matlab framework. Afterwards, the so obtained thickness will be transferred as a spatially varying resistive film to our 3D microstructure-resolved model<sup>[42,43]</sup> using the Equations outlined in Section 2.1 to investigate the impact of an inhomogeneous resistive layer. Both approaches solve mass and charge balance of the active material and the electrolyte. However, since the 3D-resolved approach takes into account individual phases or materials instead of a homogenized phase, the interface fluxes translate into volume-based source terms in the 1+1D model. The governing equations for both models are presented in Table 1. For further information, the reader is referred to the literature.<sup>[41,42,44,45]</sup> In the 1+1D model, one can use one representative particle diameter or account for different particle sizes by using a particle size distribution. We show the general

**Table 1.** Model equations for the 1 + 1D and 3D electrochemical models.

	Active material	Electrolyte
<b>1 + 1D Model</b>		
Mass balance	$\frac{\partial c_{s,n}}{\partial t} = -\frac{1}{r_n^2} \frac{\partial}{\partial r_n} (-r_n^2 D_s \frac{\partial c_s}{\partial r_n})$	$\frac{\partial (\varepsilon_e c_e)}{\partial t} = -\frac{\partial}{\partial x} (-D_e \varepsilon_e^\beta \frac{\partial c_e}{\partial x} + \frac{i_{l,i} i_e}{F}) + \frac{a_{spec} i_{BV}}{F}$
Charge balance	$0 = -\frac{\partial i_i}{\partial x} - a_{spec} i_{BV}$	$0 = -\frac{\partial i_e}{\partial x} + a_{spec} i_{BV}$
Electronic and ionic current	$i_s = -\sigma_{eff} \frac{\partial \Phi_s}{\partial x}$ $\sigma_{eff} = \sigma_{AM} \frac{\varepsilon_s}{\tau}$ $\sigma_{AM} = \frac{\sum_{n=1}^{N_{part}} \varepsilon_{PVF,n} \sigma_n}{\sum_{n=1}^{N_{part}} \varepsilon_{PVF,n}}$	$i_e = -\kappa \varepsilon_e^\beta \frac{\partial \varphi_e}{\partial x} - \kappa_D \varepsilon_e^\beta \frac{\partial c_e}{\partial x}$ $\kappa_D = \frac{2\kappa R T (t_{l,i} - 1)}{F c_e} (1 + \frac{\partial \ln f_{l,i}}{\partial \ln c_e})$
<b>3D Model</b>		
Mass balance	$\frac{\partial c_s}{\partial t} = -\nabla \cdot (-D_s \nabla c_s)$	$\frac{\partial c_e}{\partial t} = -\nabla \cdot (-D_e \nabla c_e + \frac{i_{l,i} i_e}{F})$
Charge balance	$0 = -\nabla \cdot i_s$	$0 = -\nabla \cdot i_e$
Electronic and ionic current	$i_s = -\sigma \nabla \Phi_s$	$i_e = -\kappa \nabla \varphi_e - \kappa_D \nabla c_e$ $\kappa_D = \frac{\kappa (t_{l,i} - 1)}{F} (\frac{\partial \mu_e}{\partial c_e})$
Interface	$i_{BV} = 2 i_{00} \varepsilon_{El}^{0.5} \varepsilon_{if}^{0.5} (c_{Li,max} - c_{if})^{0.5} \sinh(\frac{F}{2RT} (\Phi_s - \varphi_e - U_0(c_{if}) - R_{RS} i_{BV}))$	

predictions of our degradation model using one representative particle diameter and compare it to a case with a more realistic particle size distribution. For the latter approach, we chose five particle sizes to account for both very small particles as well as larger particles in the electrode. This is done by including the particles with different radii and particle volume fractions  $\varepsilon_{PVF}$  in the electrode, with the particle volume fractions summing up to one. Since we want to include the realistic specific surface area  $a_{spec}$  of our microstructure in the charge balance for both the one particle case as well as the particle size distribution, we need to distribute this surface area among the particles. We do that according to the theoretical specific surface areas of the individual particles. The total specific surface area is the sum of all individual particle contributions.

$$a_{spec,tot} = \sum_{n=1}^5 a_{spec,n} = \sum_{n=1}^5 a_{spec,tot} x_n \quad (14)$$

The individual weights  $x_n$  sum up to 1 and are calculated based on the theoretical specific surface area of each particle  $a_{theo,n}$ .

$$a_{theo,n} = \frac{3 \varepsilon_{PVF} \varepsilon_s}{r_n} \quad (15)$$

with  $r_n$  as the radius of each particle,  $\varepsilon_s$  as the total solid volume fraction in the electrode and  $\varepsilon_{PVF}$  as the particle volume fraction of each particle. Using the so obtained weights, the total specific surface area can be split into five individual contributions from the different particle sizes. More details can be found in the Supporting Information. In each discretization compartment, the effective conductivity for the active material charge balance is calculated as the weighted mean of all five individual conductivities. The electronic active material conductivity depends on the surface concentration.<sup>[46]</sup> Wall times for a discharge simulation range between seconds to a few minutes for the 1 + 1D model on a local computer to a few days

for the fully-resolved 3D model on a high-performance cluster using OpenMP parallelization.

### 2.2.1. Model Parametrization

We parametrize our 1 + 1D model to represent the real cathode microstructure. We calculated the specific surface area to be  $880570 \text{ m}^{-1}$ , see our previous work,<sup>[38]</sup> using the MatDict module of GeoDict 2023.<sup>[47]</sup> This includes the surface area  $a_{spec}$  between active material and the electrolyte as well as half of the surface area between active material and CBD as we assume a microporosity of 50% for this phase. Note that taking into account a specific surface area that is not based on the theoretical specific surface area of a particle in 1 + 1D requires scaling of the particle-related boundary conditions for lithium flux in the mass balance by the ratio between the specified and theoretical specific surface area to ensure mass conservation. This is needed in Eq. (13) as well as it includes the same lithium flux. The volume fractions for active material, CBD as well as pure electrolyte phase are a property of the electrode microstructure as obtained through FIB-SEM tomography. The particle size distribution was obtained using the MatDict module, which also yields the median diameter  $D_{50}$ . The effective electronic and ionic conductivities were taken from our previous work<sup>[38]</sup> and used to determine  $\tau$  for the active material charge balance and  $\beta$  for the mass and charge balance in the electrolyte. The calculations can be found in the Supporting Information. Furthermore, a grid convergence study to ensure numerical accuracy can also be found in the Supporting Information.

Note that although global metrics like the discharge curve are in very good agreement between the 1 + 1D and the 3D model (cf. Fig. S4 and S5), inhomogeneous concentration and potential fields cannot be captured in 1 + 1D simulations. Still, the volume-averaged models can be used as an efficient tool to

simulate many cycles with sufficient accuracy if parametrized carefully.

### 3. Results

Following the workflow outlined in Figure 1, we discuss the predicted film growth over cycling. Second, we investigate the impact of individual electrode and material properties on the phase transformation as well as the impact on available energy during discharge. Finally, we evaluate the impact of RS film formation in our 3D simulations.

#### 3.1. Prediction of Cycling Behavior

##### 3.1.1. First-Cycle Behavior

Figure 2a and 2b show our model predictions for oxygen loss and phase transformation in the first cycle of a 1 C constant current (CC) charge with subsequent constant voltage (CV) hold at 4.3 V with a C/20 cutoff current and subsequent CC discharge to 3.6 V. Details on the CCCV-cycling protocol are given in the Supporting Information. At a certain state-of-lithiation, which correlates approximately to a half-cell cathode voltage of 4.3 V, the outer layer of the particle starts to deteriorate and oxygen is released. The thickness of the transformed layer and the

corresponding cell voltage for one exemplary cycle are shown in Figure 2a and the resulting oxygen flux out of the cathode active material is shown in Figure 2b. Note that the different lines show the different positions in the electrode, i.e. the predicted thickness and oxygen release differ across the thickness of the electrode. The flux of oxygen starts to increase once the critical state-of-charge (soc) is reached, which results in an increase of reconstructed layer thickness. This, in turn, leads to a decrease in oxygen flux at the end of the CV phase. The film thickness increases until the end of the CV phase and remains constant upon the subsequent discharge as the time spent in the high-voltage regime is very short. Note that our simulations can therefore also predict capacity fade induced by storage at high voltages and oxygen release is not limited to cyclic aging.

Similar dynamics for the oxygen flux have been measured by Dose et al.,<sup>[8]</sup> who held a NMC cathode at a high potential for 40 h and measured the resulting gas evolution products CO, CO<sub>2</sub> and O<sub>2</sub> over time. As suggested in the Ref. [1,48], the evolved oxygen can react with EC to form CO and CO<sub>2</sub>. This allows us to relate the measured CO<sub>2</sub> and CO signals to our simulated oxygen flux. The reported shape of the resulting CO<sub>2</sub> and CO curves resemble the one of our evolved oxygen in the first cycle, thereby serving as an experimental indicator for our predictions. Already in the first simulated cycle it is clearly visible that the layer growth differs over the thickness of the electrode. Close to the separator, both oxygen flux and phase reconstruction are initiated first as this part of the electrode is

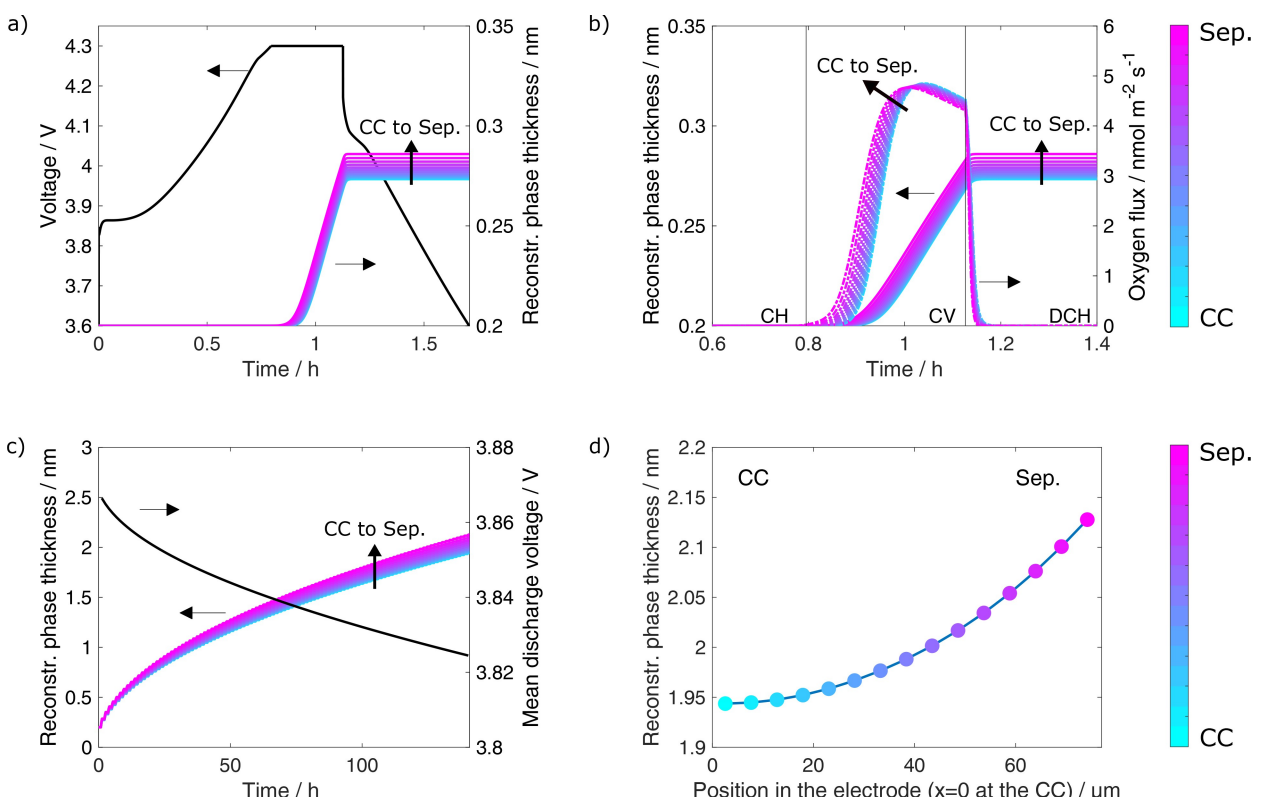


**Figure 2.** a) Growth of reconstructed layer during first cycle with voltage profile. b) Oxygen flux associated with the phase transformation in the first cycle. c) Long-term thickness growth and mean discharge voltage. d) Thickness profile of reconstructed layer after 100 cycles from (c) spatially resolved from current collector (CC) to separator (Sep.). Colors indicate the position in the electrode for all plots with turquoise at the CC and pink at the separator.

delithiated first in the charging process. The other regions start subsequently, which results in a spatial gradient in layer thickness over the electrode. The predicted film thickness is smallest at the current collector and increases towards the separator. Freiberg et al.<sup>[18]</sup> investigated the onset of oxygen release at different C-Rates and observed an earlier onset of oxygen evolution when cycled at C/10 instead of C/30, which they attributed to a local inhomogeneity of the SOC at higher currents. Our model confirms that such inhomogeneities can occur due to transport processes and highlights their importance when studying degradation.

### 3.1.2. Long-Term Cycling

Looking at the long-term growth described in Eq. (9), we expect an increase in layer growth with the square root of time. Indeed we observe this feature in our model as shown in Figure 2c. The spread across the electrode in layer thickness can also be clearly seen and even increases over time. This spread is caused by inhomogeneous lithiation across the electrode. At the same time, the oxygen flux decreases over time as the oxygen diffusion through the forming layer limits its further growth. The thickness profile across the electrode at the end of 100 cycles is shown in Figure 2d in more detail, with the lowest thickness at the current collector and the highest thickness at the separator. The total difference between those two points is approximately 0.2 nm. Transport properties are therefore of great importance for cathode design.

The additional resistance leads to a decreasing mean discharge voltage as shown in Figure 2c. The charge-averaged discharge-voltage is calculated as suggested in Ref. [1] to monitor the electrode polarization over cycling:

$$\bar{V} = \frac{\int V dq_{\text{dch}}}{\int dq_{\text{dch}}} \quad (16)$$

As the layer thickness increases, the mean discharge voltage decreases by around 42 mV. The decrease is qualitatively in line with reported decreasing mean discharge voltages,<sup>[1]</sup> even though the decrease is less pronounced. The actual loss of active material due to the phase transformation is very small in our simulation (< 0.02 mAh cm<sup>-2</sup>), see Supporting Information for details on the calculation, and therefore negligible. In our model we assume RS growth on the surfaces of secondary particles. Previous work has found indications for rocksalt phase formation on primary particles<sup>[6]</sup>, which would result in a significantly larger specific surface area available for surface degradation and thus a higher impact on capacity loss than the one predicted by our model. Furthermore, cracking can occur during cycling, which exposes fresh surface to electrolyte and further reconstruction would be expected.<sup>[12,49]</sup>

## 3.2. Influence of Structural Properties and Transport Processes

In a second step we study the influence of structural properties on film growth of the resistive film as well as the resulting energy density upon discharge. This energy is calculated as  $E = \int V dq_{\text{dch}}$  and is comprised of both losses in capacity as well as the discharge voltage. As the resistive film lowers the capacity and the mean discharge voltage,<sup>[1]</sup> the total energy that can be obtained in a cycle decreases. We investigate the resistive film properties itself as well as geometric, kinetic and transport properties of the cathode and the separator. To calculate a sensitivity for each parameter, we use the film thickness as well as the energy obtained in the last discharge after 100 cycles. The model parameters are increased individually by 10% following an One-Factor-At-A-Time Approach (OFAT) compared to the baseline case and sensitivity was calculated by Eq. (17).

$$\text{sensitivity} = \frac{X_p - X_{p,0}}{X_{p,0}} \quad (17)$$

A positive sensitivity corresponds to a thicker film or more energy than in the baseline case and, vice versa, a negative value to a thinner film or less energy. Due to arising inhomogeneity of the film thickness, we compare the minimum, mean and maximum thickness that occur in the electrode. Furthermore, we apply the sensitivity to the duration of the CV phase as well as the duration below the critical Li concentration (11950.03 mol m<sup>-3</sup>, SOC 23.9%) at the separator and the current collector. The formation energy of oxygen vacancies turns negative at a SOC of 22.5%, but due to the Sigmoid form of Eq. (8), there is no sharp start of the transformation at the critical SOC but a smooth transition that starts at slightly higher states of lithiation (cf. Figure 1). Further details are given in the Supporting Information. Therefore, we defined the critical SOC (and thus Li concentration) based on the SOC at which 5% of the maximum mobile concentration has been reached. The results are shown in Figure 3 for layer thickness, discharge energy as well as duration of the CV phase and time spent below the critical Li concentration.

### 3.2.1. Cycling Protocol

The cycling protocol can have a significant impact on the resistive film growth. For example the duration of the CV phase and the applied current density determine how long the electrode is exposed to critical conditions. Having a CV phase with a current-based cutoff allows for equilibration inside the particles (almost) regardless of the resistance. Therefore, one mainly finds differences in the film growth due to shorter or longer CV phases caused by the individual parameters. Often parameters influence heterogeneity in the cell which directly affects the length of the CV phase. Therefore, the length of the CV phase is indicative of RS formation. We present it as a separate parameter in Figure 3c). In contrast to that, a very short CV phase (or none at all) shows significant differences in

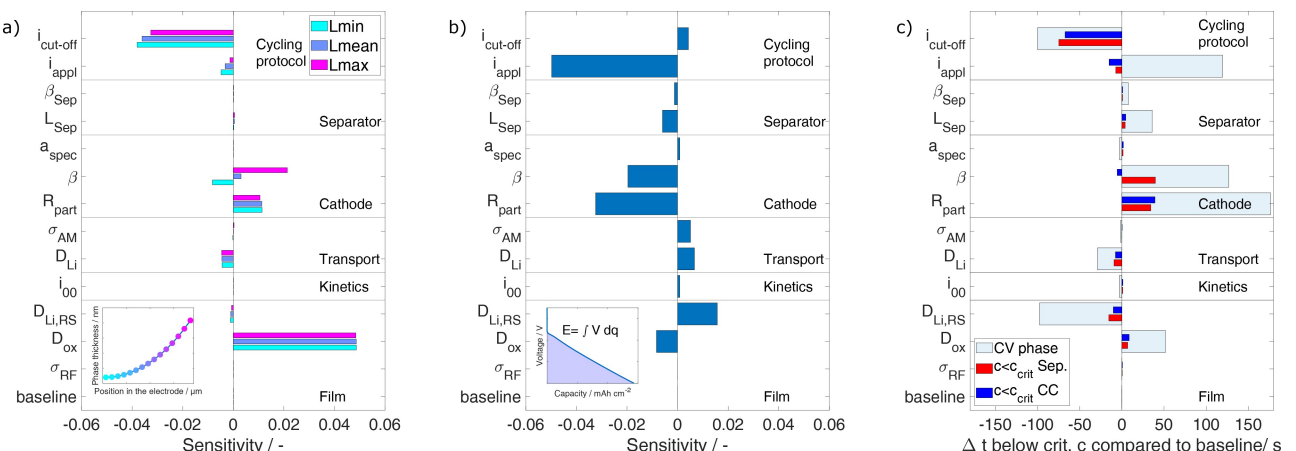


**Figure 3.** a) Sensitivity of reconstructed film thickness after 100 cycles and b) Available energy in the last discharge after 100 cycles and c) Duration of CV phase as well as duration spent below critical concentration at the separator and current collector compared to the baseline case.

the importance of individual cathode or geometric parameters on the resulting layer. A sensitivity analysis for a very short CV phase (100 s) is presented in the Supporting Information. As CCCV charging is the predominant cycling protocol, the sensitivity analysis with a realistic CCCV protocol and a C/20 cutoff is shown in Figure 3 and will be discussed in the following paragraphs.

A higher current density  $i_{appl}$  leads to slightly smaller layer thickness, while the available energy decreases strongly. Increasing the current-based CV phase cutoff leads to a significantly thinner rocksalt phase compared to the baseline case, while the available energy only increases slightly. To understand the influence of each parameter on the film thickness, we compare the total duration of the CV phase in Figure 3c) as well as the total duration of the regions next to the separator and current collector spent below the critical concentration.

Interestingly, a longer CV phase does not necessarily lead to a thicker film as shown by the total duration below the critical concentration. A higher applied current density extends the total CV phase duration by approximately 100 s compared to the baseline case due to larger concentration gradients in the active material. However, the total duration spent at low concentrations next to the current collector is nonetheless smaller, which leads to a slightly thinner resistive film in this region (cf. minimum film thickness in Figure 3a). The cutoff current leads to both significantly shorter CV phases as well as shorter periods of exposure to critical conditions for both regions. Both factors mitigate film formation. This, in turn, lowers concentration polarization and reduces the decrease in charge-transfer kinetics and therefore increases the achievable energy.

### 3.2.2. Film Properties

The diffusion coefficient of oxygen  $D_{ox}$  in the rocksalt structure has the largest impact on the film thickness growth (as

expected from Eq. (9)). A smaller oxygen diffusion coefficient thereby poses a hindrance to oxygen diffusion out of the particle, thus preventing (or slowing down) further phase transition. Despite its importance for accurate predictions of the layer growth, the diffusion coefficient is very difficult to obtain experimentally and is thus estimated in the present study. The available energy (Figure 3b) decreases with a higher oxygen diffusion coefficient due to the thicker resistive film. This, in turn, hinders Li diffusion and increases the cathode overpotential. The diffusion coefficient of Li in the rocksalt layer  $D_{Li,RS}$  only plays a minor role for the thickness growth in Figure 3a), since its influence on the layer growth is purely indirect by changing the Li concentration at the particle surface. However, it influences the available discharge energy noticeable as a higher Li diffusion coefficient in the rocksalt phase leads to better intercalation kinetics. Therefore, the concentration overpotential is smaller. The electronic conductivity  $\sigma_{RF}$  of the resistive film plays a negligible role both for the layer growth as well as the discharge energy. Note that this analysis is conducted in comparison to our baseline case and literature values for pure NiO range from the applied  $4 \cdot 10^{-6} \text{ S/cm}$ <sup>[50]</sup> to  $1 \cdot 10^{-13} \text{ S/cm}$ .<sup>[51]</sup> The electronic conductivity is assumed to be very low as NiO is known to be an electronic insulator. However, the electronic conductivity is chosen to be as low as the minimum electronic conductivity of the active material as we consider it an effective parameter comprising regions of very low conductivity as well as possibly pristine spots without any degradation, thus making it difficult to estimate.

### 3.2.3. Kinetic and Transport Properties

Next, we will focus on transport parameters in the cathode, namely the diffusion coefficient of Li in the intact active material  $D_{Li}$  as well as its electronic conductivity  $\sigma_{AM}$ . A higher Li diffusion in the active material leads to a smaller resistive film since the concentration inside the particle can equilibrate faster. Therefore, the overall current during the CV phase decreases

faster and reaches the cutoff current earlier. This translates to a shorter CV phase, see previous discussion. The electronic active material conductivity  $\sigma_{AM}$  does not influence the film thickness notably, but it is evident that it plays an important role for the available energy. This is in line with our previous study<sup>[38]</sup> suggesting a limitation of the performance of the present cathode due to an insufficient conductive network. The exchange current density  $i_{00}$  does not affect the film thickness growth or the available energy significantly.

### 3.2.4. Geometric Properties

Our simulations predict the geometry of the cathode microstructure to be an important factor in the phase transformation. First, a larger NCM particle radius  $R_{part}$  leads to a stronger film growth because the diffusion length in the particle influences the CV phase as discussed for the diffusion coefficient. Interestingly, a strong inhomogeneity for the  $\beta$ -case is observed with a lower film thickness near the current collector and a higher film thickness near the separator. This is also reflected by the duration below the critical concentration in Figure 3c). A higher Bruggeman coefficient  $\beta$  results in a smaller effective diffusion coefficient and a smaller effective ionic conductivity in the electrolyte, which impacts the performance especially at higher C-Rates such as 1 C. This leads to the decreased discharge energy in Figure 3b). A decreased conductivity and diffusion in the electrolyte result in a longer CV phase due to larger gradients, but the larger gradient also results in a lower concentration adjacent to the separator. The region next to the separator is significantly longer below the critical concentration resulting in a larger film thickness. In regions next to current collector the opposite trend is observed. This highlights the importance of transport processes for degradation studies. As shown in our previous work, performance and energy density of a commercial cathode could be improved for small current densities through addition of more CBD. However, this significantly affects ionic transport at high C-Rates. Our model predicts an even stronger inhomogeneity in film growth for

such a case. Note that changing the Bruggeman coefficient  $\beta$  by 10% changes the resulting effective parameters by 20% in the electrolyte mass and charge balance. However, since we discuss qualitative trends the same (but slightly less pronounced) result would be expected for changing the overall transport coefficients by 10%. The effective ionic transport in the separator ( $\beta_{sep}$ ) and its thickness ( $L_{sep}$ ) do not influence the thickness of the resistive layer.

### 3.3. Particle Size Distribution

As shown in the sensitivity analysis, the particle radius and thus Li diffusion in the particle can affect degradation processes. Therefore, we want to study a more realistic particle size distribution for our electrode with five particle sizes shown in Figure S2 in the Supporting Information. The considered particle diameters range from 1.76  $\mu\text{m}$  to 15.752  $\mu\text{m}$ . Figure 4 shows the layer thickness of the five individual particles considered in our analysis. Due to inhomogeneities across the cell, we observe the spatial inhomogeneity of the layer thickness as well. For the sake of clarity, the area between the minimum and maximum layer thickness for each particle is shaded uniformly in this case. The thickness profiles across the electrode for each particle size are shown in Figure S7 in the Supporting Information. The global mean of all the individual particles over time increases to approximately 2.25 nm, while the thickness of the rocksalt layer for one representative particle was below 2 nm.

Interestingly, the thickness increases with decreasing radius opposed to what the sensitivity analysis predicted for a single radius. To explain this effect, Figure 4b) shows the concentration profiles of the region next to the current collector during the first CV phase. The smallest particles delithiate the fastest and fall below the critical concentration first. The larger particles reach this threshold later, therefore they are not exposed to the critical condition as long as the small particles. However, as shown by the local current density acting on each particle in Figure 4b), the small particles equilibrate very fast while the

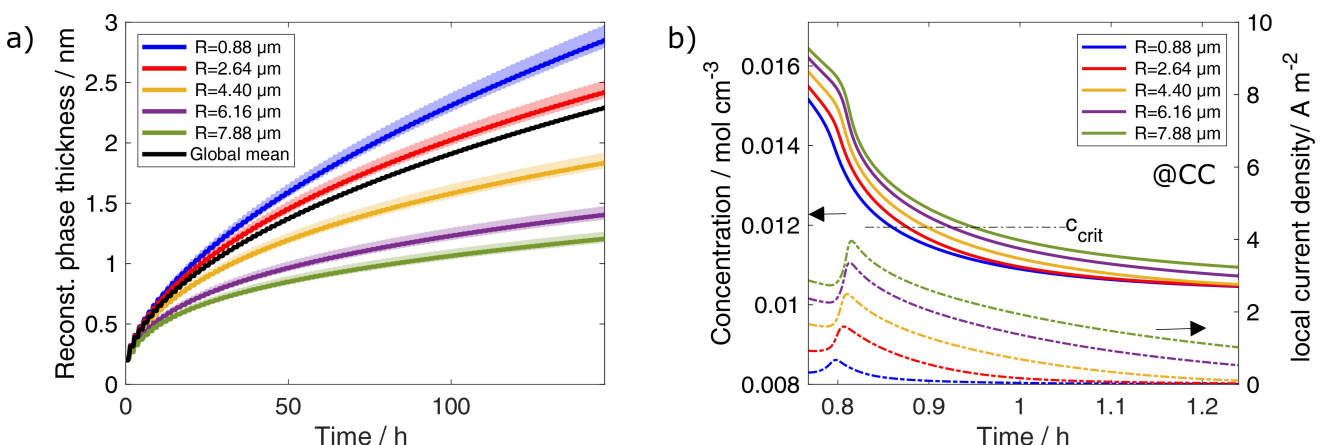


**Figure 4.** a) Resistive layer growth over time for the five different particles with global mean. b) Concentration profiles and local current densities during the first CV phase near CC.

larger particles still have a significant current density. Therefore, one can conclude that the larger particles determine the length of the CV phase, which leads to a long exposure of the smaller particles to critical conditions and thus a stronger reconstruction of active material. This study highlights that the microstructure of the electrode is crucial to understand and mitigate this degradation process. A broad particle size distribution can thereby be disadvantageous for the degradation as the large particles prolong the CV phase and have large diffusion pathways for Li. Therefore, smaller particles and a narrow PSD would be favorable for fast charging as well. A more detailed analysis of the influence of particle size distributions is subject to future work.

### 3.4. Impact of Resistive Film in Complex 3D-Microstructure

Finally, after predicting the film thickness using our 1+1D approach, we can use the so obtained thickness profiles as input for the resistive film model in 3D simulations. Figure 5 compares the discharge-capacity curves of a pristine cathode and one with the resistive film after 100 cycles. The presence of a resistive layer leads to a significant drop in capacity and voltage. The predicted capacity fade is in good agreement with the predicted capacity loss from our 1+1D model, as further discussed in the Supporting Information. Note that other degradation mechanism might contribute to experimentally observed capacity fade as well. A cathode-electrolyte-interphase (CEI) as well as particle cracking have also been attributed to capacity fade in the past. While our growth model specifically predicts the growth of the reconstructed layer, the resistive film model could be used to describe the impact of CEI as well. Therefore, it would result in similar degradation, depending on the estimated thickness and conductivity. The presented model approaches do not capture volume expansion due to de-/lithiation and the resulting mechanical stress on the material, which might lead to particle cracking as another important degradation process. While a loss of contact of some active particle regions would result in capacity loss, it is plausible that

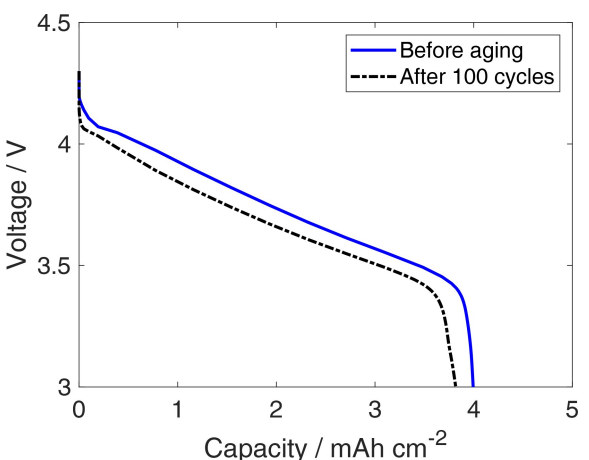


**Figure 5.** Simulated half-cell discharge curves at 1 C before aging without a resistive film and after 100 cycles with the resistive film from Figure 2.

cracking would allow even more surface reconstruction due to the higher surface area. This would lead to an even higher capacity fade and overpotential. We can account for a higher surface area in the 1+1D-model, while our fully resolved 3D-approach would need tomographic data that resolves cracks to estimate their impact. As it is not fully understood which degradation mechanisms are the most detrimental, we focus on rocksalt formation in this work as it could also be the initiation step for several follow-up reactions.

To gain an insight into the impact of a rocksalt layer, the 3D microstructure-resolved model allows us to have a closer look at the Li distribution in the structure. Figure 6 shows the concentration distribution of the electrode structures at the end of lithiation (at 3 V) in the pristine state without any resistive film and after 100 cycles. The strong concentration gradient with a very high state-of-lithiation next to the current collector can be attributed to a transport limitation of the lithiation process due to an insufficient conduction network through the CBD phase.<sup>[38]</sup> However, in the case with a resistive film the region next to the current collector is slightly less lithiated (as indicated by a less red shading in the 3D plot). Figure 6 further shows a snapshot taken from the middle plane of the 3D-structure for better visualization. For the cycled case, a lower Li concentration next to the current collector is clearly visible as well as a slightly higher lithiation at the separator. Furthermore, especially larger particles show a larger concentration gradient in the case with a resistive film as Li intercalation has been reduced throughout the whole lithiation process due to the additional resistance. This is also visualized by the concentration histograms in Figure 6 for each slice in the electrode, i.e. 0 µm corresponds to the separator and 77 µm to the current collector. The minimum, mean and maximum concentration

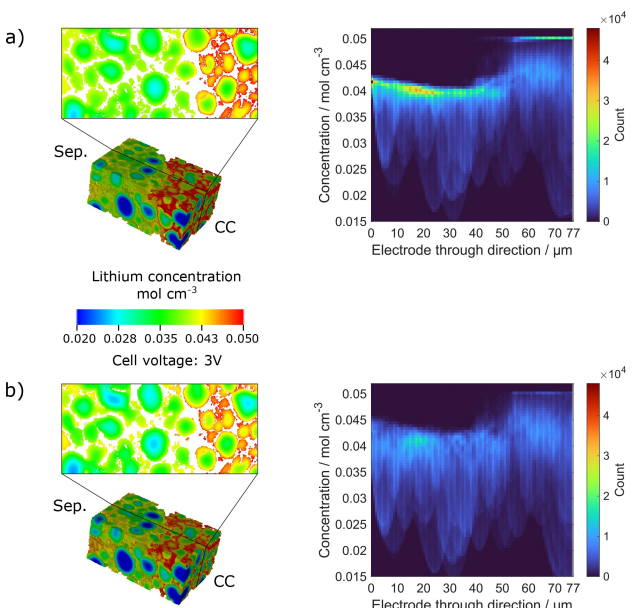


**Figure 6.** a) Concentration profile and cutout from indicated plane without film at the end of lithiation at 3 V as well as concentration histogram b) Concentration profile and cutout from indicated middle-plane with resistive film at the end of lithiation at 3 V as well as concentration histogram. See online version for best color.

values are also shown in the Supporting Information. However, they do not allow for a detailed insight into the actual Li distribution as single voxels with a certain state of lithiation influence maximum and minimum values. The concentration histograms show that in the resistive film case the maximum concentration at the separator is indeed higher compared to the pristine case, but the occurrence of these concentrations is very low. At the current collector, the overall lithiation is slightly lower, which can be seen by the count of maximum concentration at  $0.050060 \text{ mol cm}^{-3}$ . As we impose a constant current boundary condition, the lower lithiation at the current collector is compensated by a slightly higher lithiation of the rest of the electrode. However, this redistribution only affects some of the surface voxels and is therefore not very pronounced. In general, the lithiation with a resistive film seems more homogeneous compared to the case without the resistive layer. In that case, a very strong peak is observed near the maximum concentration, which reflects the overall higher state of lithiation and thus capacity.

In summary, 3D microstructure-resolved simulations can shed light on the effect of a resistive film on Li and current distribution due to individual microstructure features like a distributed CBD phase. While 1+1D models offer an efficient tool to perform several cycles, they don't capture the detailed physical transport processes accurately. In this work we combine the two approaches to gain complementary insights.

## 4. Conclusions

We have presented a modeling approach to describe a layered-to-rocksalt phase transformation of NMC accompanied by loss of lattice oxygen. To describe these processes, we apply a multi-scale modeling approach. First, we use an efficient 1+1D model that is informed by atomistic simulations to simulate cycling and growth of a reconstructed rocksalt layer. In a second step, we use this film thickness as input for our 3D microstructure-resolved simulation framework. The resistive film interface model is used in both 1+1D and 3D simulations to describe the effect of the rocksalt phase. To ensure accurate predictions by the 1+1D model, we carefully extract geometric parameters from a commercial Ni-rich electrode obtained through FIB-SEM tomography for parametrization.

We were able to show first-cycle behavior with an oxygen diffusion-limited growth of the reconstructed layer and predicted an oxygen flux in line with experimental observations. Over long-term cycling, the resistive film is predicted to grow with the square root of time, which leads to a continuous decrease in mean discharge voltage and capacity. The influence of model parameters and electrode properties was investigated regarding both the resistive film thickness as well as the available discharge energy, which is influenced by both the capacity loss and the voltage drop. We pointed out the importance of transport processes for cathode degradation as well as a strong influence of the cycling protocol. Furthermore, the diffusion coefficient of oxygen in the formed phase is of great importance, but is very hard to estimate since the exact

phases as well as the transformation process are not known or fully understood yet.

From a design perspective, a particle size distribution instead of one particle size showed how broad distributions can influence the degradation as large particles extended the CV phase, while small particles were exposed to critical concentrations longer. Therefore, a unimodal, narrow particle size distributions would be beneficial to minimize rocksalt layer growth. Simulations on a complex 3D microstructure predict a significant capacity fade as well as a lithium redistribution in the active material due to a resistive film. Further model development requires a deeper understanding of the phase transformation process by either experiments or atomistic simulations. Nonetheless, our model points out the importance of electrode properties and microstructure especially with regards to transport processes e.g. at high current densities. These insights can be used to refine material and electrode development.

## Acknowledgements

The authors thankfully acknowledge funding by the German federal ministry of education and research through the project "MiCha" (03XP0317D). The authors acknowledge support from the state of Baden-Württemberg through bwHPC and the German Research Foundation (DFG) through grant no INST 40/575-1 FUGG (JUSTUS 2 cluster). Open Access funding enabled and organized by Projekt DEAL.

## Conflict of Interests

The authors have no conflict of interest to declare.

## Data Availability Statement

The data that support the findings of this study are available from the corresponding author upon reasonable request.

**Keywords:** degradation • electrochemistry • interfaces • microstructure • oxygen loss

- [1] R. Jung, M. Metzger, F. Maglia, C. Stinner, H. A. Gasteiger, *J. Electrochem. Soc.* **2017**, *164*, A1361.
- [2] S. Oswald, H. A. Gasteiger, *J. Electrochem. Soc.* **2023**, *170*, 030506.
- [3] S.-K. Jung, H. Gwon, J. Hong, K.-Y. Park, D.-H. Seo, H. Kim, J. Hyun, W. Yang, K. Kang, *Adv. Energy Mater.* **2014**, *4*, 1300787.
- [4] R. Jung, M. Metzger, F. Maglia, C. Stinner, H. A. Gasteiger, *J. Phys. Chem. Lett.* **2017**, *8*, 4820.
- [5] B. Strehle, F. Friedrich, H. A. Gasteiger, *J. Electrochem. Soc.* **2021**, *168*, 050512.
- [6] F. Friedrich, B. Strehle, A. T. S. Freiberg, K. Kleiner, S. J. Day, C. Erk, M. Piana, H. A. Gasteiger, *J. Electrochem. Soc.* **2019**, *166*, A3760.
- [7] F. Lin, I. M. Markus, D. Nordlund, T.-C. Weng, M. D. Asta, H. L. Xin, M. M. Doeff, *Nat. Commun.* **2014**, *5*, 3529.
- [8] W. M. Dose, I. Temprano, J. P. Allen, E. Björklund, C. A. O'Keefe, W. Li, B. L. Mehdi, R. S. Weatherup, M. F. L. de Volder, C. P. Grey, *ACS Appl. Mater. Interfaces* **2022**, *14*, 13206.

- [9] B. Strehle, S. Solchenbach, M. Metzger, K. U. Schwenke, H. A. Gasteiger, *J. Electrochem. Soc.* **2017**, *164*, A2513.
- [10] J. Zhu, S. Sharifi-Asl, J. C. Garcia, H. H. Iddir, J. R. Croy, R. Shahbazian-Yassar, G. Chen, *ACS Appl. Energ. Mater.* **2020**, *3*, 4799.
- [11] J. Zheng, T. Liu, Z. Hu, Y. Wei, X. Song, Y. Ren, W. Wang, M. Rao, Y. Lin, Z. Chen, J. Lu, C. Wang, K. Amine, F. Pan, *J. Am. Chem. Soc.* **2016**, *138*, 13326.
- [12] H.-H. Ryu, G.-T. Park, C. S. Yoon, Y.-K. Sun, *Small (Weinheim an der Bergstrasse, Germany)* **2018**, *14*, e1803179.
- [13] N.-Y. Park, G.-T. Park, S.-B. Kim, W. Jung, B.-C. Park, Y.-K. Sun, *ACS Energy Lett.* **2022**, *7*, 2362.
- [14] M. D. Radin, S. Hy, M. Sina, C. Fang, H. Liu, J. Vinckeviute, M. Zhang, M. S. Whittingham, Y. S. Meng, A. van der Ven, *Adv. Energy Mater.* **2017**, *7*, 1602888.
- [15] C. Xu, K. Märker, J. Lee, A. Mahadevegowda, P. J. Reeves, S. J. Day, M. F. Groh, S. P. Emge, C. Ducati, B. Layla Mehdi, C. C. Tang, C. P. Grey, *Nat. Mater.* **2021**, *20*, 84.
- [16] W. M. Dose, W. Li, I. Temprano, C. A. O'Keefe, B. L. Mehdi, M. F. L. de Volder, C. P. Grey, *ACS Energy Lett.* **2022**, *7*, 3524.
- [17] D. Streich, C. Erk, A. Guéguen, P. Müller, F.-F. Chesneau, E. J. Berg, *J. Phys. Chem. C* **2017**, *121*, 13481.
- [18] A. T. S. Freiberg, S. Qian, J. Wandt, H. A. Gasteiger, E. J. Crumlin, *ACS Appl. Mater. Interfaces* **2023**, *15*, 4743.
- [19] C. Misiewicz, R. Lundström, I. Ahmed, M. J. Lacey, W. R. Brant, E. J. Berg, *J. Power Sources* **2023**, *554*, 232318.
- [20] J. Wandt, A. T. Freiberg, A. Ogrodnik, H. A. Gasteiger, *Mater. Today* **2018**, *21*, 825.
- [21] R. Jung, P. Strobl, F. Maglia, C. Stinner, H. A. Gasteiger, *J. Electrochem. Soc.* **2018**, *165*, A2869.
- [22] A. T. S. Freiberg, M. K. Roos, J. Wandt, R. de Vivie-Riedle, H. A. Gasteiger, *J. Phys. Chem. A* **2018**, *122*, 8828.
- [23] P. Yan, J. Zheng, J.-G. Zhang, C. Wang, *Nano Lett.* **2017**, *17*, 3946.
- [24] J. Zheng, P. Yan, J. Zhang, M. H. Engelhard, Z. Zhu, B. J. Polzin, S. Trask, J. Xiao, C. Wang, J. Zhang, *Nano Res.* **2017**, *10*, 4221.
- [25] N. Y. Kim, T. Yim, J. H. Song, J.-S. Yu, Z. Lee, *J. Power Sources* **2016**, *307*, 641.
- [26] T. R. Tanim, Z. Yang, A. M. Colclasure, P. R. Chinnam, P. Gasper, Y. Lin, L. Yu, P. J. Weddle, J. Wen, E. J. Dufek, I. Bloom, K. Smith, C. C. Dickerson, M. C. Evans, Y. Tsai, A. R. Dunlop, S. E. Trask, B. J. Polzin, A. N. Jansen, *Energy Storage Mater.* **2021**, *41*, 656.
- [27] N.-Y. Park, H.-H. Ryu, G.-T. Park, T.-C. Noh, Y.-K. Sun, *Adv. Energy Mater.* **2021**, *11*, 2003767.
- [28] Y.-S. Kang, S. Y. Park, K. Ito, Y. Kubo, Y. Shin, D. Y. Kim, D.-H. Seo, S. Kim, J.-H. Park, S.-G. Doo, M. Koh, J. A. Seo, K. Park, *J. Power Sources* **2021**, *490*, 229542.
- [29] S. Watanabe, M. Kinoshita, T. Hosokawa, K. Morigaki, K. Nakura, *J. Power Sources* **2014**, *258*, 210.
- [30] H. Zhang, B. M. May, F. Omenya, M. S. Whittingham, J. Cabana, G. Zhou, *Chem. Mater.* **2019**, *31*, 7790.
- [31] A. R. Genreith-Schreiver, H. Banerjee, A. S. Menon, E. N. Bassey, L. F. Piper, C. P. Grey, A. J. Morris, *Joule* **2023**, *7*, 1623.
- [32] F. Kong, C. Liang, L. Wang, Y. Zheng, S. Perananthan, R. C. Longo, J. P. Ferraris, M. Kim, K. Cho, *Adv. Energy Mater.* **2019**, *9*, 1802586.
- [33] K. Min, S.-W. Seo, Y. Y. Song, H. S. Lee, E. Cho, *Phys. Chem. Chem. Phys.* **2017**, *19*, 1762.
- [34] C. Cai, D. Zhang, Q. Zhang, K. Chen, W. Hua, C. Peng, D. Xue, *J. Chem. Phys.* **2023**, *158*, 114703.
- [35] A. Ghosh, J. M. Foster, G. Offer, M. Marinescu, *J. Electrochem. Soc.* **2021**, *168*, 020509.
- [36] M. Zhuo, G. Offer, M. Marinescu, *J. Power Sources* **2023**, *556*, 232461.
- [37] D. Zhuang, M. Z. Bazant, *J. Electrochem. Soc.* **2022**, *169*, 100536.
- [38] A. Lindner, S. Both, W. Meneskou, S. Hein, T. Danner, A. Latz, U. Krewer, *Batteries & Supercaps* **2024**, *7*, e202400503.
- [39] J. C. García, J. Bareño, J. Yan, G. Chen, A. Hauser, J. R. Croy, H. Iddir, *J. Phys. Chem. C* **2017**, *121*, 8290.
- [40] M. Clausnitzer, M. Ihrig, L. Cressa, S. Hein, M. Finsterbusch, S. Eswara, L.-Y. Kuo, T. Danner, P. Kaghazchi, D. Fattakhova-Rohlfing, O. Guillou, A. Latz, *Energy Storage Mater.* **2024**, *67*, 103262.
- [41] M. Doyle, T. F. Fuller, J. Newman, *J. Electrochem. Soc.* **1993**, *140*, 1526.
- [42] A. Latz, J. Zausch, *J. Power Sources* **2011**, *196*, 3296.
- [43] Fraunhofer Institute for Industrial Mathematics, BEST – Battery and Electrochemistry Simulation Tool. <https://www.itwm.fraunhofer.de/best>, last accessed: 05.12.2024.
- [44] T. Danner, M. Singh, S. Hein, J. Kaiser, H. Hahn, A. Latz, *J. Power Sources* **2016**, *334*, 191.
- [45] W. T. John Newman, *AIChE J.* **1975**, *21*, 25.
- [46] T. Knorr, S. Hein, B. Prifling, M. Neumann, T. Danner, V. Schmidt, A. Latz, *Energies* **2022**, *15*, 7821.
- [47] Math2Market GmbH, GeoDict simulation software Release 2023.
- [48] L. Hartmann, L. Reuter, L. Wallisch, A. Beiersdorfer, A. Adam, D. Goldbach, T. Teufel, P. Lamp, H. A. Gasteiger, J. Wandt, *J. Electrochem. Soc.* **2024**, *171*, 060506.
- [49] S. Lee, L. Su, A. Mesnier, Z. Cui, A. Manthiram, *Joule* **2023**, *7*, 2430.
- [50] O. A. Ali, M. A. Hameed, Q. G. Al-Zaidi, *Trans. Indian Nat. Acad. Eng.* **2020**, *5*, 27.
- [51] A. R. West, *Basic Solid State Chem.*, Wiley, Chichester and Weinheim, 2. ed. edition 1999.

Manuscript received: December 19, 2024

Revised manuscript received: February 13, 2025

Accepted manuscript online: February 17, 2025

Version of record online: March 12, 2025